



Strain gradient effects in periodic flat punch indenting at small scales



K.L. Nielsen^{a,*}, C.F. Niordson^a, J.W. Hutchinson^b

^a Department of Mechanical Engineering, Solid Mechanics, Technical University of Denmark, DK-2800 Kgs. Lyngby, Denmark

^b School of Engineering and Applied Sciences, Harvard University, 29 Oxford Street, Cambridge, MA 02138, USA

ARTICLE INFO

Article history:

Received 17 January 2014

Received in revised form 15 May 2014

Available online 14 June 2014

Keywords:

Higher order theory

Size effects

Indentation

Imprinting

ABSTRACT

Experiments on soft polycrystalline aluminum have yielded evidence that, besides the required punch load, both the size and shape of imprinted features are affected by the scale of the set-up, e.g. substantial details are lost when the characteristic length is on the order of 10 μm . The objective of this work is to clarify the role played by strain gradients on this issue, and to shed light on the underlying mechanisms. For this, indentation by a periodic array of flat punch indenters is considered, and a gradient enhanced material model that allows for a numerical investigation of the fundamentals are employed. During a largely non-homogeneous deformation, the material is forced up in between the indenters so that an array of identical imprinted features is formed once the tool is retreated. It is confirmed that the additional hardening owing to plastic strain gradients severely affects both the size and shape of these imprinted features. In particular, this is tied to a large increase in the mean contact pressure underneath the punch, which gives rise to significant elastic spring-back effects during unloading.

© 2014 Elsevier Ltd. All rights reserved.

1. Introduction

Flat punch indenting of elastic–plastic solids has earned renewed interest in recent years as a way of rapidly mass producing micron surface features. To achieve high throughput, the surface punching has been evolved into a continuous micro-manufacturing process that relies on imprinting/molding by rolling (referred to as roll-molding, (Lu and Meng, 2013)). However, the underlying mechanisms remains the same. In its simplest form, a flat patterned indenter is pressed into the underlying material and thereby leaving an imprint in the plastically deformed surface once retreated. This classical problem is well-established in the literature, not the least owing to the slip-line field solutions for an rigid perfectly plastic solid by Hill (1950), which has been verified in numerical studies employing conventional plasticity (Nepershin, 2002). Their efforts, along with corresponding studies on pyramidal (Vickers or Knoop), spherical (Brinell) and wedge indentation, have yielded important in-sight into the underlying mechanics, and indentation has become a widely used standard technique in material testing at all scales. It is, however, recognized that indenting at small scales results in increased yield resistance, for materials that deform plastically by dislocation movement, when compared to large scale testing.

When employing indenting (or punching) for manufacturing purposes, the surface imprint is often aimed to represent a counterpart to the indenter as closely as possible. However, a perfect match is complicated by effects such as elastic spring-back, strain gradient hardening, material inertia, and viscosity. Redesign of the punch may improve the imprint, but in general perfectly sharp edges cannot be achieved and some surface curvature must be accepted; this with little noticeable different at large scales. However, deviations from perfectly sharp edges become increasingly evident when the punching process is down-scaled to do micro-manufacturing. Unfortunately, the goal of attaining sharp edges, and abrupt variations in the deformed geometry, are associated with large strain gradients, which lead to the before mentioned increased hardening at micron scale. The explanation for this is now generally accepted to lie in the concept of Geometrically Necessary Dislocations (GND's). When large plastic strain gradients appear GND's must be stored (Ashby, 1970), and this gives rise to free energy associated with the local stress field of the GND's, as well as increased dissipation when the GND's move in the lattice. At small scales, GND's can become a substantial portion of the total dislocation density which is normally dominated by so-called Statistically Stored Dislocations (SSD's) at larger scale. Thus, a larger amount of energy is required to deform the material at small scales in the presence of gradients, and this leads to an apparent increase in yield stress and strain hardening. To accurately predict the shape and size of imprints made during micro-manufacturing the

* Corresponding author. Tel.: +45 4525 4258; fax: +45 4593 1475.

E-mail address: kin@mek.dtu.dk (K.L. Nielsen).

employed material model must therefore represent stresses over the full range of length scales involved.

A vast amount of theoretical literature seeking to encapsulate the experimentally observed gradient effects at micron scale has been put forward, counting both phenomenological models (Aifantis, 1984; Fleck and Hutchinson, 1997, 2001; Gudmundson, 2004; Gurtin and Anand, 2005; Lele and Anand, 2008; Fleck and Willis, 2009a,b), and micro-mechanics based models (Gao et al., 1999; Huang et al., 1999; Gurtin, 2002; Qiu et al., 2003). The higher order theory by Fleck and Willis (2009b) is employed in the current study, and the concept of higher order stresses, work conjugate to the strain gradients, is thus adopted to widen the range of length scales for which the model is valid. The objective is to model an experiment on soft polycrystalline aluminum at small scale, where the impression made by a periodic array of micro-indenters deviates substantially from that observed at larger scales. Through numerical modeling it is the aim to clarify the influence of plastic strain gradients. Moreover, by including unloading the elastic spring-back can be quantified when compared to the surface shape at maximum indentation depth. By choosing a material length parameter of $L_D = 1 \mu\text{m}$, it is demonstrated that significant gradient effects should be expected for imprinted features with a characteristic length on the order of $10 \mu\text{m}$ and below. This choice of length parameter are in line with the estimates for the length parameter put forward by Hutchinson (2000) ($L_D \approx 0.25 - 5 \mu\text{m}$, depending on the gradient type being stretch or rotational), and recently by Danas et al. (2012) ($L_D \approx 0.5 - 1.5 \mu\text{m}$).

The paper is structured as follows. The considered boundary value problem is summarized in Section 3, while the material model formulation and numerical procedure are briefly outlined in Sections 2 and 4. A modeling framework capable of predicting the rate-independent material response is employed, and the results are laid out in Section 5. Focus is on shape and size changes to the imprints made onto the plastically deformed surface, as well as on changes to the loading history due to strain gradient effects. Some concluding remarks are given in Section 6.

2. Strain gradient material models

In spite of indentation being an inherent finite strain problem, a small strain version of the strain gradient plasticity theory by Fleck and Willis (2009b) (tensorial version) is employed in this study as a first approximation. This is considered sufficient for the small indentation depths analyzed. A compact summary of the rate-independent model formulation published by Nielsen and Niordson (2013, 2014) is given below. Throughout, Einstein's summation rule is utilized in the tensor equations and $()_{,i}$ denotes partial differentiation with respect to the spatial coordinate x_i .

2.1. Fundamentals of the Fleck–Willis strain gradient theory

A small strain formulation is employed. The total strain rate is determined from the gradients of the displacement rates; $\dot{\epsilon}_{ij} = (\dot{u}_{i,j} + \dot{u}_{j,i})/2$, and decomposed into an elastic part, $\dot{\epsilon}_{ij}^e$, and a plastic part, $\dot{\epsilon}_{ij}^p$, so that; $\dot{\epsilon}_{ij} = \dot{\epsilon}_{ij}^e + \dot{\epsilon}_{ij}^p$. For a higher order gradient dependent material, involving higher order stresses, the principle of virtual work reads (Gudmundson, 2004)

$$\int_V (\sigma_{ij} \delta \epsilon_{ij} + (q_{ij} - s_{ij}) \delta \epsilon_{ij}^p + \tau_{ijk} \delta \epsilon_{ij,k}^p) dV = \int_S (T_i \delta u_i + t_{ij} \delta \epsilon_{ij}^p) dS. \quad (1)$$

Here, σ_{ij} is the symmetric Cauchy stress tensor, and $s_{ij} = \sigma_{ij} - \delta_{ij} \sigma_{kk}/3$ its deviatoric part. In addition to conventional stresses, the principle of virtual work incorporates the so-called

micro-stress tensor, q_{ij} (work-conjugate to the plastic strain, ϵ_{ij}^p), and the higher order stress tensor, τ_{ijk} (work-conjugate to plastic strain gradients, $\epsilon_{ij,k}^p$). The right-hand side of Eq. (1) thereby includes both conventional tractions, $T_i = \sigma_{ij} n_j$, and higher order tractions, $t_{ij} = \tau_{ijk} n_k$, with n_k denoting the outward normal to the surface S , which bounds the volume V .

The mechanisms associated with dislocation movement and/or storage of geometrically necessary dislocations (GND's) (Ashby, 1970; Gurtin, 2002; Ohno and Okumura, 2007) have been incorporated into the current higher order theory by assuming the micro-stress, q_{ij} , and higher order stresses, τ_{ijk} , to have a dissipative part only, such that; $q_{ij} = q_{ij}^D$, and $\tau_{ijk} = \tau_{ijk}^D$. Thus, assuming the form of the free energy to be

$$\Psi = \frac{1}{2} (\epsilon_{ij} - \epsilon_{ij}^p) \mathcal{L}_{ijkl} (\epsilon_{kl} - \epsilon_{kl}^p) \quad (2)$$

the conventional stresses are derived as; $\sigma_{ij} = \partial \Psi / \partial \epsilon_{ij}^e = \mathcal{L}_{ijkl} (\epsilon_{kl} - \epsilon_{kl}^p)$, where \mathcal{L}_{ijkl} is the isotropic elastic stiffness tensor. In this study, all energetic gradient contributions are omitted. The dissipative stress quantities in the plastic regions read (Gudmundson, 2004; Fleck and Willis, 2009b)

$$q_{ij}^D = \frac{2}{3} \frac{\sigma_c}{\dot{E}^p} \dot{\epsilon}_{ij}^p, \quad \text{and} \quad \tau_{ijk}^D = \frac{\sigma_c}{\dot{E}^p} (L_D)^2 \dot{\epsilon}_{ij,k}^p \quad (3)$$

with σ_c and \dot{E}^p identified as the effective stress and the associated effective plastic strain rate, respectively, given by

$$\sigma_c = \sqrt{\frac{3}{2} q_{ij}^D q_{ij}^D + (L_D)^{-2} \tau_{ijk}^D \tau_{ijk}^D}, \quad \text{and} \quad \dot{E}^p = \sqrt{\frac{2}{3} \dot{\epsilon}_{ij}^p \dot{\epsilon}_{ij}^p + (L_D)^2 \dot{\epsilon}_{ij,k}^p \dot{\epsilon}_{ij,k}^p}. \quad (4)$$

Here, $\dot{\epsilon}_{ij,k}^p$ is the gradient of the plastic strain rates, and L_D is the dissipative length parameter which is included for dimensional consistency. The quantities defined in Eqs. (3) and (4) only exists in the plastic regions (in which $\sigma_c = \sigma_F$), while $q_{ij}^D = q_{ij} = s_{ij}$ in the elastic regions, such that the effective stress reduces to the conventional von Mises stress. An isotropic power hardening material is modeled in the present work, with the current flow stress given by

$$\sigma_F[E^p] = \sigma_y \left(1 + \frac{E^p}{\sigma_y/E} \right)^N \quad (5)$$

Here, E is Young's modulus, N is the strain hardening exponent, and σ_y is the initial yield stress. The material parameters used in the simulations are given in Table 1.

To complete the higher order theory, Fleck and Willis (2009b) put forward two minimum principles that delivers the incremental solution to the displacement rate field, \dot{u}_i , and plastic strain rate field, $\dot{\epsilon}_{ij}^p$.

Assume that the current stress/strain state is known in terms of the displacement, u_i , and plastic strain, ϵ_{ij}^p , fields. The plastic strain rate field, in the subsequent load increment, is thereby determined as; $\dot{\epsilon}_{ij}^p = \lambda \dot{\epsilon}_{ij}^{p*}$, where the plastic trial field, $\dot{\epsilon}_{ij}^{p*}$, follows from the minimum statement (Minimum Principle I in Fleck and Willis, 2009b)

Table 1
Mechanical properties.

Parameter	Significance	Value
σ_y/E	Uniaxial yield strain	0.001
ν	Poisson's ratio	0.3
N	Strain hardening exponent	0.05–0.2

$$H = \inf_{\dot{\epsilon}_{ij}^{p*}} \int_V (\sigma_F[E^p] \dot{\epsilon}^{p*} - s_{ij} \dot{\epsilon}_{ij}^{p*}) dV - \int_S t_{ij} \dot{\epsilon}_{ij}^{p*} dS \quad (6)$$

and λ is the plastic multiplier associated with the trial field. It is noticed that a solution to the plastic trial field is obtained independently of the incremental solution to the displacement field associated with incremental loading. Thus, only the plastic multiplier, λ , links the two, but remains unknown at this stage of the solution.

To make this link, [Fleck and Willis \(2009b\)](#) formulated the following functional to be minimized (Minimum Principle II)

$$J[\dot{u}_i, \lambda \geq 0] = \frac{1}{2} \int_V (\mathcal{L}_{ijkl} (\dot{\epsilon}_{ij} - \dot{\epsilon}_{ij}^p) (\dot{\epsilon}_{kl} - \dot{\epsilon}_{kl}^p) + h[E^p] \dot{E}^p) dV - \int_S (\tilde{T}_i \dot{u}_i + \dot{t}_{ij} \dot{\epsilon}_{ij}^p) dS. \quad (7)$$

The minimum principles deliver the solution for the displacement rates and the multiplier associated with the plastic trial field, $\dot{\epsilon}_{ij}^{p*}$. Here, $\dot{\epsilon}_{ij}^p = \lambda \dot{\epsilon}_{ij}^{p*}$ and $\dot{E}^p = \lambda \dot{E}^{p*}$ in Eq. (7), whereas, the current hardening modulus is determined by $h[E^p] = d\sigma_F/dE^p$.

A corresponding rate-dependent model formulation was laid out by [Fleck and Willis \(2009b\)](#), while its comparison to the current rate-independent version can be found in [Nielsen and Niordson \(2013, 2014\)](#).

3. Problem formulation

[Fig. 1](#) illustrates the considered model set-up, where flat punch indentation by a periodic array of equally spaced indenters is parameterized. The set-up is chosen so that it also resembles a 2D cross-sectional cut of the mold-rolling process newly studied by [Lu and Meng \(2013\)](#). Thus, besides the stationary punch indentation problem, it is the aim to bring out first indications of size effects for mold-rolling at small scales. Throughout, symmetry conditions are enforced at $x_1 = W$ ($\dot{u}_1 = 0$ and $\dot{\epsilon}_{12}^p = 0$), free sliding conditions are applied along $x_2 = 0$ ($\dot{u}_2 = 0$), periodicity is enforced at $x_1 = 0$ ($\dot{u}_1 = 0$ and $\dot{\epsilon}_{12} = 0$), and the loading is applied by prescribing a controlled displacement at $b \leq x_1 \leq W$ and $x_2 = H$ ($\dot{u}_2 = -\dot{\Delta}$, rigid indenter). The free sliding (or symmetry) condition at $x_2 = 0$ implies essentially that indentation takes place from both sides of the plate simultaneously. For flat punch indentation, this approximation deteriorates as the sheet

becomes thin compared to the indenter spacing, but it is expected to be a good model for the mold-rolling process.

To determine suitable boundary conditions for the interface between the indenter and the surface material a brief investigation of four different cases will be presented.

The four cases are;

Case A: Full sticking ($\dot{u}_1 = 0$) and constraint plastic flow ($\dot{\epsilon}_{ij}^p = 0$).

Case B: Free sliding ($T_1 = 0$) and constraint plastic flow ($\dot{\epsilon}_{ij}^p = 0$).

Case C: Full sticking ($\dot{u}_1 = 0$) and free plastic flow ($t_{ij} = 0$).

Case D: Free sliding ($T_1 = 0$) and free plastic flow ($t_{ij} = 0$).

The parameterized model set-up allows a number of dimensionless quantities to be identified, and the response for the material to be governed by

$$F = f\left(\frac{b}{W}, \frac{H}{W}, \frac{\sigma_Y}{E}, \nu, N, \frac{L_D}{W}\right) \quad (8)$$

where b is the channel width, W is the punch distance, and H is the half sheet thickness (see [Fig. 1](#)), whereas the material parameters; σ_Y , E , ν , N , and L_D has been introduced in the preceding section.

4. Numerical formulation and solution procedure

The employed numerical solution procedure rests on the general finite element approach presented in [Nielsen and Niordson \(2014\)](#), and has as basis the structure of the formulation presented by [Niordson and Hutchinson \(2011\)](#). Here, using a standard finite element interpolation of the displacement field, u_i , and the plastic strain field, ϵ_{ij}^p , respectively.

$$u_i = \sum_{n=1}^8 N_i^{(n)} U^{(n)} \quad \text{and} \quad \epsilon_{ij}^p = \sum_{n=1}^4 M_{ij}^{(n)} \epsilon^{p(n)} \quad (9)$$

where $N_i^{(n)}$ are quadratic shape functions, $M_{ij}^{(n)}$ are linear shape functions, while $U^{(n)}$ and $\epsilon^{p(n)}$ holds the nodal values of the unknown variables.

The incremental procedure for this strain gradient model formulation consists of two successive steps, in which “Step 1” determines the plastic strain rate field from Minimum Principle I based on the known stress/strain conditions in the current state (in terms of the displacement field, u_i , and the plastic strain field, ϵ_{ij}^p). “Step 2” subsequently determines the corresponding incremental displacement solution, as well as the plastic multipliers for the rate-independent formulation, from Minimum Principle II. Full details on the numerical implementation and solution procedure for the rate-independent formulation can be found in [Nielsen and Niordson \(2013, 2014\)](#).

5. Results

The aspect ratio of the periodic domain considered remains fixed at $H/W = 0.5$ for all the results presented, unless otherwise specified. Together with the symmetry conditions at $x_2 = 0$, this models periodic punch indentation (or approximates mold-rolling) from both sides onto a sheet of thickness $2H$.

Punch response curves are shown in [Fig. 2](#) in terms of the mean contact pressure under the punch as a function of indentation depth, Δ , normalized by the half sheet thickness, H . Results are shown for a fixed ratio of channel width to indenter distance of $b/W = 0.3$, and material parameters chosen according to [Table 1](#). An intermediate strain hardening exponent is chosen ($N = 0.1$)

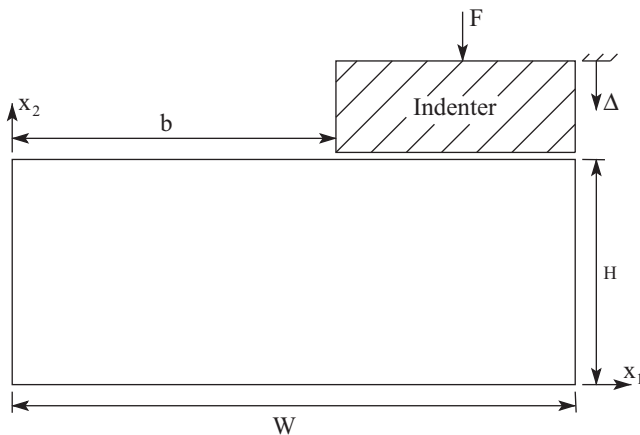


Fig. 1. Schematic of a flat punch indenter pressed into a strain gradient enhanced elastic-plastic material. The setup will be employed to study the response to a periodic array of indenters (symmetry conditions at $x_1 = 0$ and $x_1 = W$).

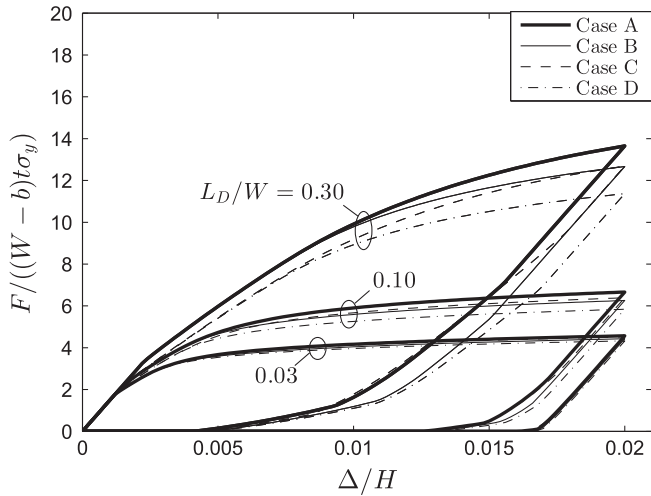


Fig. 2. Punch response curves displaying both loading and unloading of the indenter. Results are shown for $L_D/W = [0.03, 0.1, 0.3]$, for the four boundary configurations at the indenter interface; Case A ($\dot{\epsilon}_{ij}^p = 0, \dot{u}_1 = 0$), Case B ($\dot{\epsilon}_{ij}^p = 0, T_1 = 0$), Case C ($t_{ij} = 0, \dot{u}_1 = 0$), and Case D ($t_{ij} = 0, T_1 = 0$). Here, $N = 0.1, b/W = 0.3$, and $H/W = 0.5$.

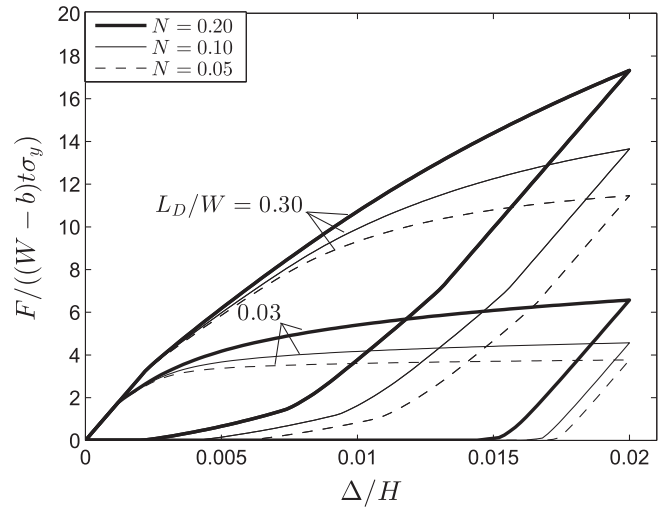


Fig. 3. Punch response curves showing the effect of conventional strain hardening and hardening owing to plastic strain gradients. Results are shown for $L_D/W = [0.03, 0.3]$, $N = [0.05, 0.1, 0.2]$, and $b/W = 0.3$ (Case A boundary conditions, and $H/W = 0.5$).

along with three different material length parameters, $L_D/W = [0.03, 0.1, 0.3]$ ¹, whereof the results for the smallest length parameter closely resembles those of a conventional material. For each of the material length parameters, the four distinct boundary cases presented in Section 3 are considered, and results for all combinations of full/no friction and full/no constraint on the plastic flow at the punch interfaces are brought out in Fig. 2. It is seen that while the full constraint conditions (Case A) leads to the stiffest response, and the no constraint conditions (Case D) leads to the softest response, a full constraint on only one of the two fields (either \dot{u}_1 or $\dot{\epsilon}_{ij}^p$) yields a similar response that lie in between the two extremes. Furthermore, the results show that a significant size effect exists for the periodic punch problem in agreement with the findings by Guha et al. (2013a,b).

Throughout this work, all punch response curves are shown for both loading and unloading of the indenter (thus until the indenter has been completely retreated). It is clear that, initially unloading takes place along the same slope as that found at initial contact. However, as the contact area decreases while the indenter is retreated, the slope decreases; an effect most clearly seen for the larger values of L_D/W . It has been noticed that the indenter first loses contact with the deformed surface near the center of the channel ($x_1 = W$), whereafter this detached region spreads and eventually reaches the corners of the indenter at $x_1 = b$.

In the following studies only Case A (full friction and constraint plastic flow) for the interface condition at the punch is considered, as this gives rise to the highest peak load (though only small differences are predicted between Cases A–D).

The effect of conventional material hardening is presented in Fig. 3, where results for $N = [0.05, 0.1, 0.2]$ are shown for two values of the material length parameter, $L_D/W = [0.03, 0.3]$. While conventional hardening clearly influences the response, it is obvious that gradient hardening dominates, and even the case with low conventional hardening ($N = 0.05$) exhibits very strong hardening due to strain gradients – in particularly for $L_D/W = 0.3$.

The channel shape, in terms of the outline of the deformed top surface, is presented in Figs. 4 and 5 upon complete removal of the punch after indentation. Results are shown for three different length parameters, $L_D/W = [0.03, 0.1, 0.3]$, and for two ratio of channel width to indenter spacing, $b/W = [0.3, 0.8]$. For a length parameter that yields results close to the conventional limit ($L_D/W = 0.03$), a flat channel is produced with a ridge rising sharply where the indenter corners were in contact. This is seen for both the narrow feature ($b/W = 0.3$, compare Figs. 4a, c, and e), and the wider feature ($b/W = 0.8$, compare Figs. 4b, d, and f). However, when the material length parameter increases relative to the other geometric dimensions (or equivalently; if the scale of the geometric parameters become relative smaller), these distinct details are lost as the channel become less flat by the ridge rising less sharply after unloading (see Fig. 4). This size effect on the shape of the channel, and the imprinted feature, is the focus of this study as it complicates the process of making an accurate imprint that match the indenter counterpart.

To quantify the size effects on the imprinted feature, a parameterized model of the topology is set-up in Fig. 6. A target surface of width “b” (according to Fig. 1) is here constructed so that it matches the area underneath the curve that outlines the predicted surface. Thus, the two surfaces will coincide in case of a perfect match ($\alpha = \beta = 1$), whereas differences between the imprinted feature and the target surface can be quantified by four key measures; (i) the channel depth, δ^* , (ii) the maximum width at average height, β , (iii) the deviation from the average height, α , and (iv) the integrated mismatch between the two curves, calculated as; $\text{Error} = \int_0^W |y_{\text{def}} - y_{\text{target}}| dx / A_{\text{Deformed}}$ ². The evolution of the four parameters is shown in Figs. 7–10 for fixed length parameters, and various values of the ratio of channel width to indenter spacings, b/W , and sheet thicknesses H/W .

For fixed sheet thickness and indenter displacement, ($H/W = 0.5$ and $\Delta_0/H = 0.02$), the ratio of channel width and indenter spacing, b/W , clearly influences on the shape of the imprinted feature, which in turn is affected by the length

¹ Employing the present Fleck–Willis model framework, the numerics become unstable for $L_D \rightarrow 0$. It was found that $L_D/W = 0.03$ comes fairly close to that limit for the current set-up.

² Here, y_{def} and y_{target} are the curve describing the predicted and target imprint, respectively, and A_{Deformed} is the area underneath the curves. An example is shown in Fig. 6.

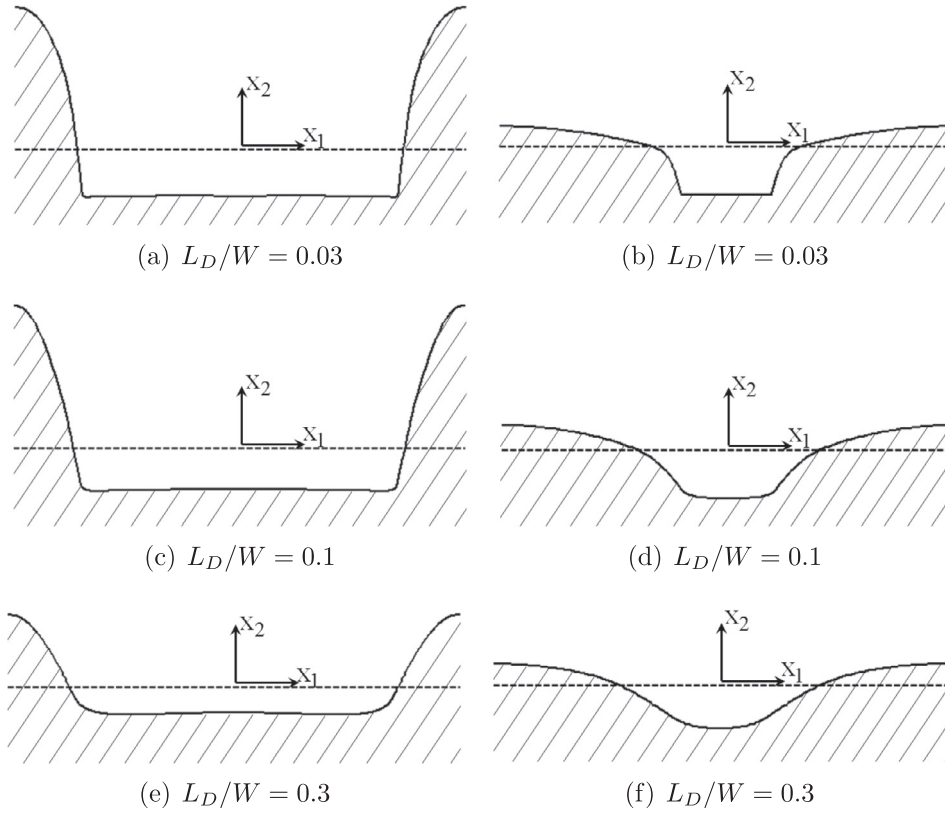


Fig. 4. Deformed top surface after unloading the indenter, where the hatched area indicates the gradient enhanced solid and the dashed line indicates the initial top surface. Results are shown for two indenter widths, $b/W = [0.3, 0.8]$, with $L_D/W = [0.03, 0.1, 0.3]$, and $N = 0.1$ (Case A boundary conditions). Here, Δ_0 is the maximum indentation depth ($\Delta_0/H = 0.02$ and $H/W = 0.5$).

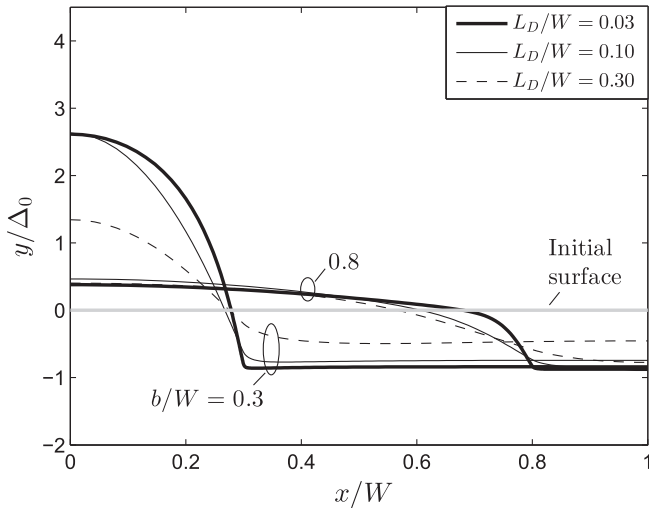


Fig. 5. Deformed top surface after unloading the indenter, here displaying the effect of strain gradients. Results are shown for two indenter widths, $b/W = [0.3, 0.8]$, and with $L_D/W = [0.03, 0.1, 0.3]$, and $N = 0.1$ (Case A boundary conditions). Here, Δ_0 is the maximum indentation depth ($\Delta_0/H = 0.02$ and $H/W = 0.5$).

parameter (thus the scale of the imprint). For $L_D/W = 0.03$, which yields a material response close to the conventional limit, it is clear that the best match to the target surface is obtained. This is concluded by; the height “ α ” being fairly close to unity for all b/W , the width “ β ” reaching the highest values detected, and the integrated error taking the lowest values (see Fig. 7). This agrees well with the deformed top surfaces shown in Figs. 4 and 5, where little

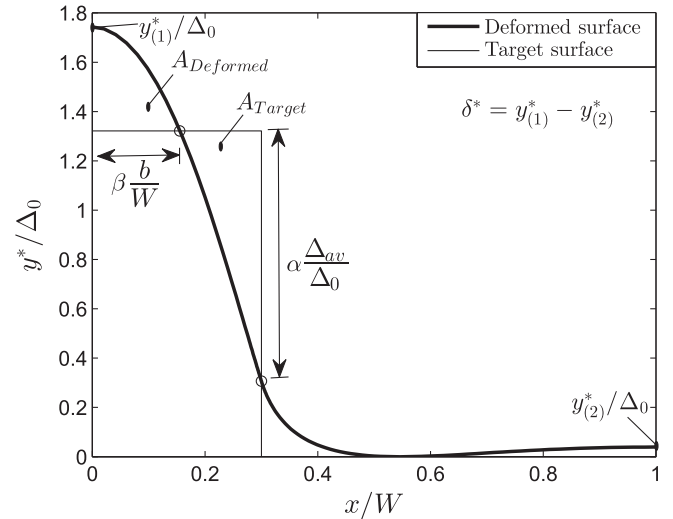


Fig. 6. Parametrization of the deformed top surface quantifying to which degree the target surface has been achieved. Here, $A_{Deformed}$ is the area underneath the curved outlining the deformed surface, and $A_{Target} = A_{Deformed}$ allows constructing the target surface for a given indenter width, b/W . For a perfect match, the intersection α and β yields; $\alpha = \beta = 1$. The final indent depth, δ^* , is also indicated. Here, Δ_0 is the maximum indentation depth ($\Delta_0/H = 0.02$ and $H/W = 0.5$).

spring-back is observed ($\alpha \approx 1$) for the smallest length parameter, and a reasonable accurate match to the target surface is obtained. However, even in the conventional limit perfectly sharp corners on the imprinted feature cannot be expected, and this deviation becomes increasingly evident for larger length parameters

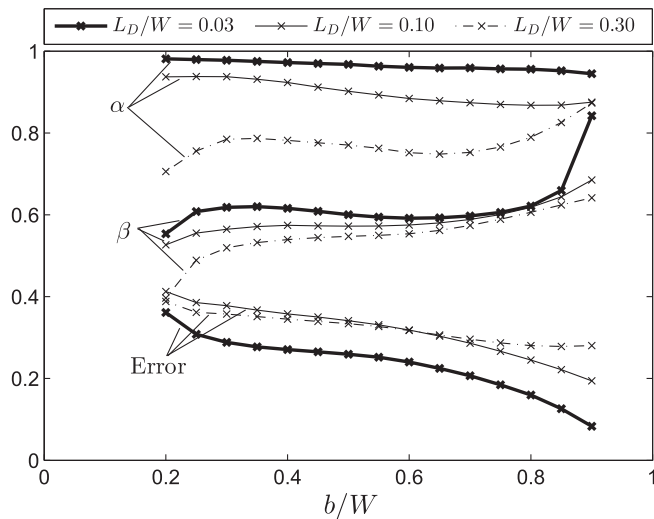


Fig. 7. Match between the deformed top surface and the target surface for various indenter widths, b/W . The match is quantified by the “ α ” and “ β ” value specified in Fig. 6, as well as the $\text{Error} = \int_0^W |y_{\text{def}} - y_{\text{target}}| dx / A_{\text{deformed}}$. Results are shown for $L_D/W = [0.03, 0.1, 0.3]$, and $N = 0.1$ (Case A boundary conditions, $H/W = 0.5$, and $\Delta_0/H = 0.02$).

(corresponding to smaller imprints). In particular for the largest length parameter, $L_D/W = 0.3$, it is obvious that; the height “ α ” has dropped significantly, the width “ β ” is lowered, and that the integrated error has increased (see Fig. 7). Thus, the imprint appears smoothed and substantial details are lost when compared to an imprint made at larger scales. Moreover, it is clear from Fig. 7 that for fixed length parameter, the match with the target surface deteriorates with increasing indenter width (b/W decreases).

In line with the above discussion, interesting results are revealed when considering the evolution of the channel depth, δ^* , with the ratio b/W , at different length scales. From Fig. 8b, it is seen that the channel depth increases monotonically for increasing indenter width (decreasing b/W) close to the conventional limit ($L_D/W = 0.03$), whereas the monotony is lost once gradient effects play a significant role. To get to grips with this, it is

important to realize that as b/W decreases, an increasing volume of material is displaced by the indenter (recall that Δ_0/H is fixed), while the constraint on the deformation increases (the free surface where the material extrudes upward becomes smaller). Thus, neglecting material compressibility, the average height of the feature, at maximum indenter depth, has to increase with decreasing b/W , and moreover the mean contact pressure under the indenter has to increase – in particular for large length parameters. This is also evident from Fig. 8a. In general, the increased mean contact pressure intensifies elastic volume changes, so that less material is forced upward, as well as adds to the elastic straining, which in turn yields larger spring-back during unloading. It is this competition between changes in the mean contact pressure and the elastic spring-back that give rise to the non-monotonic behavior in Fig. 8b.

A corresponding parametric study on the effect of changing the sheet thickness is laid out in Figs. 9 and 10. Here, keeping the ratio of channel width to indenter spacing fixed at $b/W = 0.3$ and 0.8 , respectively, and varying the length parameter to imitate imprints being made at different scales. Fig. 9b clearly shows the channel depth, δ^* , being a monotonic function of the sheet thickness, H/W . This is tied to Δ_0/H being kept constant ($=0.02$). Thus, for increasing sheet thickness, the punch travels further into the material, displacing a larger volume for fixed indenter size, and forcing more material to extrude upwards at the free surface. However, as for the above study, the final channel depth is largely affected by changes to the length parameter as large strain gradients arise with the deformation. From Fig. 9b, this is particularly evident for a wide punch ($b/W = 0.3$) as a fairly large amount of displaced material has to be extruded upward over a small span of free surface. On the other hand, the final channel depth for a narrow punch ($b/W = 0.8$) is much less sensitive to the length parameter, due to a smaller displaced volume and a relatively larger free surface.

Fig. 10 displays the four key measures identified from the parameterized surface topology in Fig. 6, as function of the normalized sheet thickness, H/W . Results are, here, presented for two ratio's of channel width to indenter spacing, $b/W = [0.3, 0.8]$. As for the above results, the best possible match to the target surface is obtained in the conventional limit (no gradient effects), while the substantial details in the surface morphology are lost for decreasing b/W .

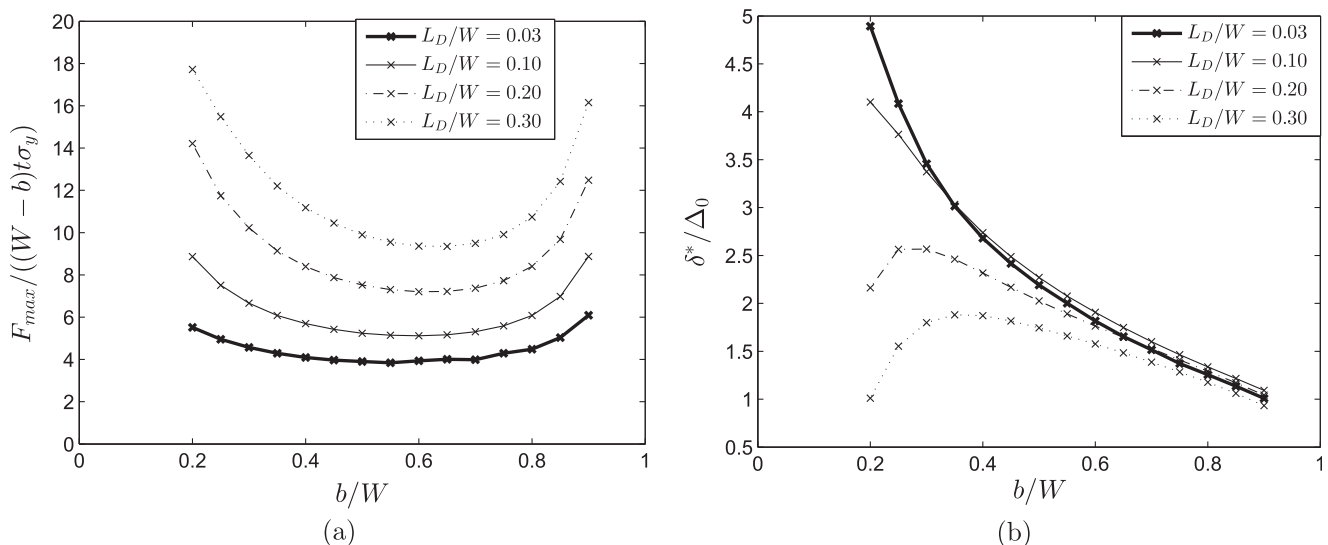


Fig. 8. Normalized a) peak load, F_{max} , and b) maximum indenter depth, δ^* , respectively, for various indenter widths, b/W , and fixed sheet thickness, $H/W = 0.5$. Results are shown for $L_D/W = [0.03, 0.1, 0.2, 0.3]$, and $N = 0.1$ (Case A boundary conditions). Here, Δ_0 is the maximum indentation depth ($\Delta_0/H = 0.02$).

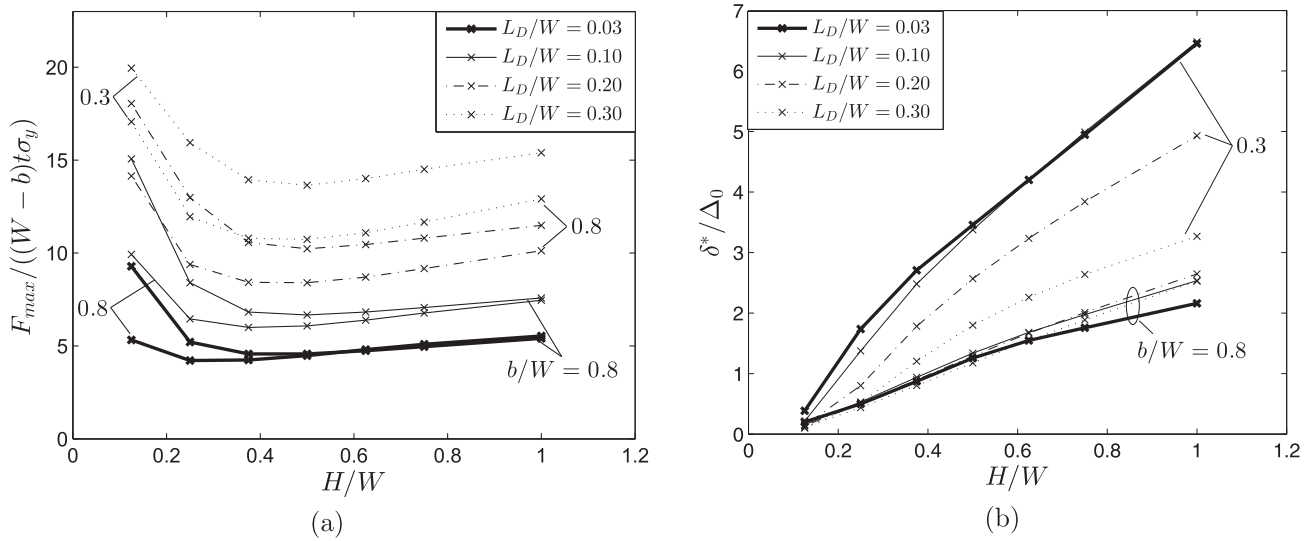


Fig. 9. Normalized (a) peak load, F_{max} , and (b) maximum indenter depth, δ^* , respectively, for various sheet thicknesses, H/W , and fixed indenter width at $b/W = 0.3$ and $b/W = 0.8$, respectively. Results are shown for $L_D/W = [0.03, 0.1, 0.2, 0.3]$, and $N = 0.1$ (Case A boundary conditions). Here, Δ_0 is the maximum indentation depth ($\Delta_0/H = 0.02$).

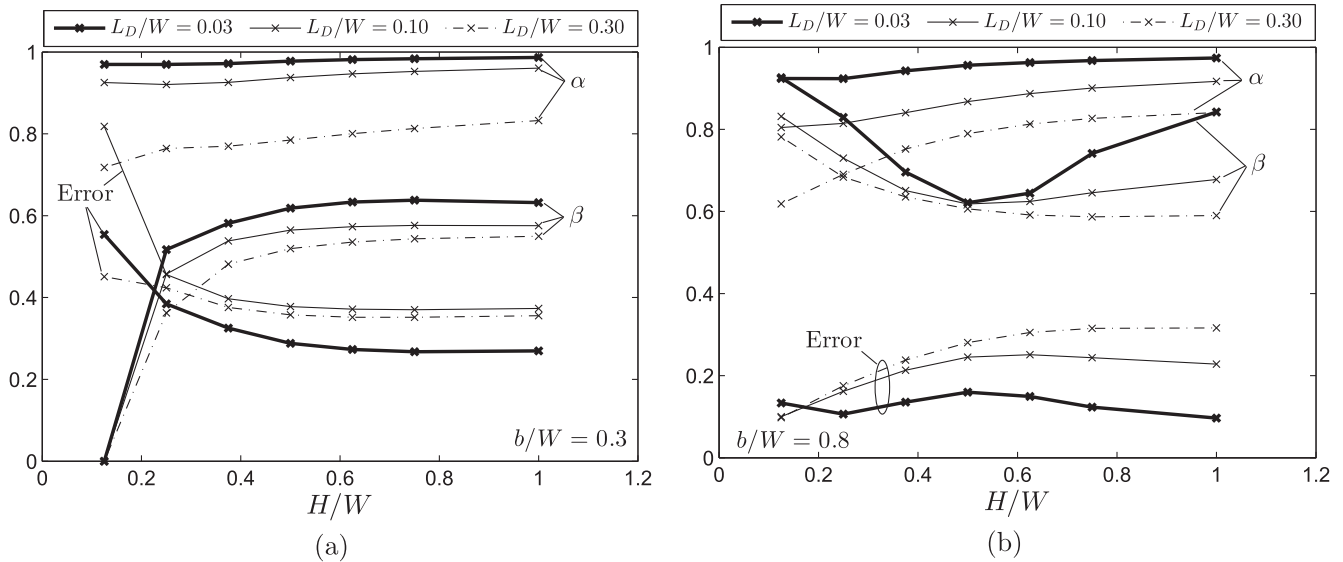


Fig. 10. Match between the deformed top surface and the target surface for various sheet thicknesses, H/W , for two indenter widths; (a) $b/W = 0.3$, and (b) $b/W = 0.8$. The match is quantified by the “ α ” and “ β ” value specified in Fig. 6, as well as the Error = $\int_0^W |y_{def} - y_{target}| dx / A_{Deformed}$. Results are shown for $L_D/W = [0.03, 0.1, 0.3]$, and $N = 0.1$ (Case A boundary conditions, and $\Delta_0/H = 0.02$).

6. Concluding remarks

Small scale indentation of elastic–plastic materials is well-known to reflect size effects, in terms of increased hardness when compared to indentation made at larger scale. Similar size effects are predicted for flat punch indentation, or imprinting of micron scale features onto sheet metals, and it is obvious from Figs. 2, 3, 8a, and 9a that the peak-load associated with a specific indentation depth rises as the length parameter increases (equivalent to down-scaling the process). The mean contact pressure underneath the punch thereby increases due to strain gradient hardening as the material show more resistance to extrude upward between the indenters. This intensifies elastic volume changes, and adds to the elastic straining, so that a larger elastic spring-back occurs during unloading (see Figs. 5 and 6). Thus, as the punch tool is retreated, the size change of a micron scale imprint is substantial (see Figs. 5,

8, and 9), and the degree of mismatch with the mold counterpart is worsened when down-scaling the process (see Figs. 7 and 10). Throughout, isotropic hardening is assumed for the material response. However, it is expected that kinematic hardening would have an influence on the observed length scale effect for the shape of the final impression as it is largely tied to the elastic spring back.

The implications of these findings can be tied directly to micro-manufacturing processes, e.g. the so-called roll-molding developed for low-cost, high-throughput of micron-scale imprints (Lu and Meng, 2013). By letting the roll hold the mold counterpart, micro-channel array imprinting on thin sheet metals poses essentially the same issues as those treated in the presented work. Thus, the shape of the imprinted features will be affected by down-scaling the process. However, shape optimization of the punch geometry could potentially improve on the imprinted feature so that a match better the desired impression.

Acknowledgements

K.L. Nielsen and C.F. Niordson are financially supported by The Danish Council for Independent Research under the research career programme Sapere Aude in the project “Higher Order Theories in Solid Mechanics”.

References

- Aifantis, E., 1984. On the microstructural origin of certain inelastic models. *J. Eng. Mater. Technol.* 106, 326–330.
- Ashby, M., 1970. The deformation of plastically non-homogeneous alloys. *Philos. Mag.* 21, 399–424.
- Danas, K., Deshpande, V., Fleck, N., 2012. Size effects in the conical indentation of an elasto-plastic solid. *J. Mech. Phys. Solids* 60, 1605–1625.
- Fleck, N., Hutchinson, J., 1997. Strain gradient plasticity. *Adv. Appl. Mech.* 33, 295–361.
- Fleck, N., Hutchinson, J., 2001. A reformulation of strain gradient plasticity. *J. Mech. Phys. Solids* 49, 2245–2271.
- Fleck, N., Willis, J., 2009a. A mathematical basis for strain-gradient plasticity theory. Part I: scalar plastic multiplier. *J. Mech. Phys. Solids* 57, 161–177.
- Fleck, N., Willis, J., 2009b. A mathematical basis for strain-gradient plasticity theory. Part II: tensorial plastic multiplier. *J. Mech. Phys. Solids* 57, 1045–1057.
- Gao, H., Huang, Y., Nix, W., Hutchinson, J., 1999. Mechanism-based strain gradient plasticity I: analysis. *J. Mech. Phys. Solids* 47, 1239–1263.
- Gudmundson, P., 2004. A unified treatment of strain gradient plasticity. *J. Mech. Phys. Solids* 52, 1379–1506.
- Guha, S., Sangal, S., Basu, S., 2013a. Finite element studies on indentation size effect using a higher order strain gradient theory. *Int. J. Solids Struct.* 50, 863–875.
- Guha, S., Sangal, S., Basu, S., 2013b. Numerical investigations of flat punch molding using a higher order strain gradient plasticity theory. *Int. J. Mater. Forum.*
- Gurtin, M., 2002. A gradient theory of single-crystal viscoplasticity that accounts for geometrically necessary dislocations. *J. Mech. Phys. Solids* 50, 5–32.
- Gurtin, M., Anand, L., 2005. A theory of strain-gradient plasticity for isotropic, plastically irrotational materials. Part I: small deformations. *J. Mech. Phys. Solids* 53, 1624–1649.
- Hill, R., 1950. *The Mathematical Theory of Plasticity*. Oxford University Press, Great Clarendon Street, Oxford, New York.
- Huang, Y., Gao, H., Nix, W., Hutchinson, J., 1999. Mechanism-based strain gradient plasticity II: analysis. *J. Mech. Phys. Solids* 48, 99–128.
- Hutchinson, J., 2000. Plasticity at the micron scale. *Int. J. Solids Struct.* 37, 225–238.
- Lele, S., Anand, L., 2008. A small-deformation strain-gradient theory for isotropic viscoplastic materials. *Philos. Mag.* 88, 3655–3689.
- Lu, B., Meng, W., 2013. Roll molding of microchannel arrays on Al and Cu sheet metals: a method for high-throughput manufacturing. *J. Micro Nano Manuf.*
- Nepershin, R., 2002. Indentation of a flat punch into a rigid-plastic half space. *J. Appl. Math. Mech.* 66, 135–140.
- Nielsen, K., Niordson, C., 2013. A 2D finite element implementation of the Fleck–Willis strain-gradient flow theory. *Eur. J. Mech. A/Solids* 41, 134–142.
- Nielsen, K., Niordson, C., 2014. A numerical basis for strain-gradient plasticity theory: rate-independent and rate-dependent formulations. *J. Mech. Phys. Solids* 63, 113–127.
- Niordson, C., Hutchinson, J., 2011. Basic strain gradient plasticity theories with application to constrained film deformation. *J. Mech. Mater. Struct.* 6, 395–416.
- Ohno, N., Okumura, D., 2007. Higher-order stress and grain size effects due to self-energy of geometrically necessary dislocations. *J. Mech. Phys. Solids* 55, 1879–1898.
- Qiu, X., Huang, Y., Wei, Y., Gao, H., Hwang, K., 2003. The flow theory of mechanism-based strain gradient plasticity. *Mech. Mater.* 35, 245–258.